Soil Biology and Biochemistry 211 (2025) 109951

Contents lists available at ScienceDirect

Soil Biology and Biochemistry

journal homepage: www.elsevier.com/locate/soilbio

The dark side of the soil carbon cycle: Hydroxyl radicals and abiotic CO_2 production

Carolina Merino [a,c,*], Ignacio Jofré [a,b], Francisco Nájera [a,c], Francisco Matus [c], Felipe Aburto [d], José Dörner [e], Rafael Rubilar [f,g], Michaela A. Dippold [h], Yakov Kuzyakov [i,j]

[a] Laboratory of Geomicrobiology, Department of Chemical Sciences and Natural Resources, Universidad de La Frontera, Temuco, Chile
[b] Scientific and Technological Bioresource Nucleus, Universidad de La Frontera, Temuco, Chile
[c] Laboratory of Conservation and Dynamics of Volcanic Soils, Department of Chemical Sciences and Natural Resources, Universidad de La Frontera, Temuco, Chile
[d] Pedology and Soil Biogeochemistry Laboratory, Department of Soil and Crop Sciences, Texas A&M University, College Station, TX, USA
[e] Instituto de Ingeniería Agraria y Suelos, Facultad de Ciencias Agrarias y Alimentarias, Universidad Austral de Chile, Valdivia, Chile
[f] Cooperativa de Productividad Forestal, Departamento de Silvicultura, Facultad de Ciencias Forestales, Universidad de Concepción, Concepción, Chile
[g] Centro Nacional de Excelencia para la Industria de la Madera (CENAMAD) – ANID BASAL FB210015, Pontificia Universidad Católica de Chile, Santiago, Chile
[h] Geo-Biosphere Interactions, Department of Geosciences, University of Tübingen, Tübingen, Germany
[i] Soil Science of Temperate Ecosystems, Agricultural Soil Science, University of Göttingen, 37077, Göttingen, Germany
[j] Bioeconomy Research Institute, Vytautas Magnus University, Agriculture Academy, Kaunas Reg., Lithuania

ARTICLE INFO

Keywords:
Dark Fenton-type reactions
Hydroxyl radicals
Ferrous iron
Dissolved organic carbon
Redox fluctuations

ABSTRACT

Fenton-type reactions without light (Dark-Fenton) in some forest soils generate hydroxyl radicals (•OH) from ferrous iron [Fe(II)] and dissolved organic carbon (DOC) under fluctuating anoxic–oxic conditions. We hypothesized that Fe(II) concentrated in micropores (<10 μm) raises radical production in soil, exceeding electron donation solely by DOC, and that radical-mediated abiotic oxidation releases CO_2. Four undisturbed humid forest soils, ranging from sandy loam to silty clay loam with contrasting parent materials, were incubated anoxically (~14 days) and then exposed to oxygen for 24 h in the dark. We introduced hydrogen peroxide (5–300 μM), and the $\delta^{13}C$ signature confirmed that the CO_2 originated from DOC rather than from bulk soil organic matter (SOM). Soils with higher Fe(II) (~35 μM) in clay-rich or metamorphic parent materials produced up to ~25 nM •OH in 24 h and released ~20–25 % additional CO_2 upon short-term re-oxygenation. Volcanic soils with ~15 μM Fe(II) generated fewer radicals (~5–10 nM) and only 5–10 % extra CO_2. Micropores concentrated Fe(II), intensifying •OH formation and drove an abiotic CO_2 flux that reached 25 % of total soil respiration. We condensed this effect into a single coefficient, ready for implementation in soil carbon models. Concluding, short redox pulses can oxidize 5–20 % of DOC via hydroxyl radicals produced by Fe(II) oxidation, adding a non-microbial (abiotic) flux to the total CO_2 released from soil. These results revise the common view that soil CO_2 originates exclusively from microbial and root respiration by revealing a sizeable abiotic contribution under fluctuating redox conditions.

1. Introduction

Soils in humid forests worldwide often remain near water saturation for extended periods due to high precipitation and low water permeability, generating microenvironments with alternating anoxic and oxic conditions (Totsche et al., 2018; Wilhelm et al., 2022). When oxygen (O_2) penetrates these anoxic microsites, iron (Fe) and dissolved organic carbon (DOC) can undergo redox reactions that release carbon dioxide (CO_2) in addition to microbial respiration (Hall and Silver, 2015; Yu and Kuzyakov, 2021). One such mechanism involves dark Fenton-type processes, where ferrous iron [Fe(II)] reacts with O_2 to form hydrogen peroxide (H_2O_2), which then generates hydroxyl radicals (•OH). These radicals can oxidize organic substrates under light-independent conditions (Wang et al., 2022; Xiao et al., 2024). The simplified steps are:

$$Fe(II) + O_2 \rightarrow H_2O_2 + Fe(III) \quad (1)$$

* Corresponding author. Laboratory of Geomicrobiology, Department of Chemical Sciences and Natural Resources, Universidad de La Frontera, Temuco, Chile.
E-mail address: carolina.merino@ufrontera.cl (C. Merino).

https://doi.org/10.1016/j.soilbio.2025.109951
Received 18 July 2025; Accepted 17 August 2025
Available online 18 August 2025

$$H_2O_2 + Fe(II) \rightarrow \cdot OH + OH^- + Fe(III) \quad 2$$

$$\cdot OH + DOC \rightarrow CO_2 + \text{other oxidation products} \quad 3$$

Studies in aquatic and wetland environments show that aromatic domains and reduced functional groups in DOC facilitate electron transfer to O_2, fueling H_2O_2 production (Page et al., 2013b; Ayeni et al., 2022). In other soils, changes in biodiversity and iron mobilization can also shift H_2O_2 content (Yu et al., 2019). Residual Fe(II) then drives the second reaction, forming •OH that rapidly oxidizes DOC or other organic matter pools (Hu et al., 2023; Wen et al., 2023). These processes have been recognized in water-saturated sediments (Zhao et al., 2021), but their magnitude and controlling micro-scale drivers in upland soils that experience frequent redox oscillations remain poorly understood (Wilmoth, 2021).

Soil texture strongly influences the pore-size distribution as well as water flow and saturation (Dörner et al., 2015, 2016; Dec et al., 2017). Sandy soils contain large macropores with rapid drainage yet low water-holding capacity, whereas clayey soils are dominated by micropores that retain water longer. Sub-10 μm micropores in humid forest soils often remain water-filled, concentrating Fe(II) and DOC in the absence of O_2 until intermittent aeration introduces O_2 (Keiluweit et al., 2017; Totsche et al., 2018). This cycle can occur over hours or days, leading to repeated radical formation events.

Although microbial respiration has historically been viewed as the dominant CO_2 source in soils, recent work suggests that dark Fenton-type reactions can oxidize a noticeable fraction of DOC in soils with high Fe content (Matus et al., 2019; Merino et al., 2020a, 2020b). Texture also modulates belowground carbon (C) pools and nutrient availability in highly weathered forests, highlighting the role of micropores in C and Fe cycling (Silver et al., 2000; Barcellos et al., 2018; Lin et al., 2022). However, no study has yet quantified how pore-scale Fe(II) distributions measured by X-ray μCT translate into hydroxyl radical yields and abiotic CO_2 fluxes during natural redox pulses. The fraction of total CO_2 derived from dark Fenton-type oxidation at field-relevant timescales, however, remains a knowledge gap (Xiao et al., 2024; Barcellos et al., 2025).

These uncertainties include whether the oxidized C originates solely from DOC or includes bulk soil organic matter (SOM). Experiments with isotope labeling enable differentiating carbon sources *in-situ* (Whalen et al., 2022). These dark Fenton-type pathways may represent an unaccounted mechanism of soil C loss, especially under changing rainfall patterns or temperature regimes that boost redox oscillations (Liu et al., 2023b; Wang et al., 2024).

Herein, we integrated three advances to address this gap. First, X-ray μCT was used to quantify the aggregated microporosity and Fe(II) enrichment. Second, high-resolution probes track Fe(II), H_2O_2, and •OH during anoxic–oxic shifts. Third, natural-abundance $\delta^{13}C$ traces the emitted CO_2 in intact forest soil cores. We hypothesize that Fe(II) pooled in <10 μm pores drives •OH bursts after O_2 pulses, adding ≥5 % abiotic CO_2 to the total flux. We further derived a scaling coefficient so that process-based soil-C models can incorporate this abiotic term. The study aims to (i) quantify the •OH production from Fe(II) and DOC under anoxic–oxic transitions and (ii) determine the share of DOC oxidation that contributes to non-microbial CO_2 release in humid forest soils. By resolving pore-scale controls and providing a model-ready coefficient, we refined the current concepts of soil respiration and C-cycle feedback in landscapes with fluctuating redox regimes.

2. Methodology

2.1. Study sites, soil sampling and characterization analyses

Four soils were selected from humid forests in south-central Chile, where human disturbance is minimal. Their textures (sandy loam to clay loam) coincide with distinct parent materials: volcanic ash in sandy soils (SL, SCL) vs. granite/metamorphic rocks in finer soils (SiCL, CL), making it difficult to separate the effects of texture from those of lithology (Table 1). The 0–5 cm organic horizon was removed at each site, and samples were collected from the Ah mineral horizon (5–15 cm). The soil material was placed in sterile bags, transported, and stored at ~5 °C until analysis.

Soil texture was determined using the hydrometer method after organic matter (OM) was destroyed by treatment with H_2O_2 (Dörner et al., 2015). Cation exchange capacity (CEC) was calculated from the total exchangeable bases (Mg, Ca, K, Na), extracted with 1 mol L^{-1} NH_4OAc at pH 7.0, and analyzed using flame atomic absorption spectrophotometry. Soil pH was measured in suspensions with deionized water at a 1:2.5 (w/v) ratio (Palma et al., 2016). Total Fe content was determined by acid digestion and analyzed by atomic absorption spectroscopy (Moursy et al., 2020).

The stable carbon isotopic composition ($\delta^{13}C$) of DOC and bulk soil organic carbon (SOC) was measured by isotope ratio mass spectrometry (IRMS; Thermo Fisher Scientific, Bremen, Germany). DOC was extracted from fresh soil with ultrapure water (1:10, w/v), filtered (0.2 μm), and freeze-dried prior to analysis. SOC content was measured after oven-drying at 105 °C and finely grinding a separate soil subsample. Both DOC and SOC samples were combusted in an elemental analyzer (Flash EA1112) interfaced to the IRMS (Delta plus XP IRMS). Analytical precision was ±0.12 ‰ (n = 20 standards), and duplicate soil subsamples diverged by ≤ 0.18 ‰.

2.2. Micro-CT scanning and pore-size mapping

Blocks of soil (~0.45 m × 0.22 m) were air-dried and broken into smaller pieces (~5 mm aggregates). For each soil type, 4–6 replicates were scanned with a SkyScan 1273 X-ray microtomograph (Bruker, Kontich, Belgium) at 100 kV, using an Al + Cu filter to harden the beam. The voxel size was ~9 μm, capturing pore diameters from ~2.5 μm to 10 μm. Approximately 940 projections were acquired in 0.2° increments (0–180°), with a total scan time of ~2 h per image. Pre-test scans (n = 3 per soil) comparing intact, water-saturated cores with gently air-dried aggregates at the same voxel size showed a porosity difference of 1.8 ± 0.7 % (p = 0.34). NRecon® (Bruker) generated three-dimensional volumes for each replicate.

Pore spaces were identified by applying intensity thresholds, focusing on microzones <10 μm where anoxia may develop (Keiluweit et al., 2018; Totsche et al., 2018). A 2D slice of each volume was exported as a voxel-intensity matrix. In R, intensities were converted into approximate pore diameters (μm) and visualized with a color scale from 2.5 to 10.0 μm (red for larger pores, blue for smaller). The resulting microporosity (<10 μm) was expressed as a volume-weighted fraction (%) and later used to normalize Fe(II) stocks in each soil.

2.3. Extraction and characterization of dissolved organic carbon (DOC)

A soil subsample was mixed with ultrapure water (1:10 w/v) for 24 h in the dark. The suspension was filtered at 0.2 μm to obtain water-extractable organic matter (WEOM) (Merino et al., 2017). DOC was measured with a total organic carbon (TOC) analyzer (TOC-L CPH, Shimadzu, Japan). A UV-3600 dual-beam spectrophotometer (Shimadzu, Japan) scanned each WEOM sample from 200 to 700 nm. The absorbance at 254 nm was normalized by the DOC concentration to calculate the specific UV absorbance ($SUVA_{254}$, L mg^{-1} m^{-1}), an indicator of aromaticity. Fluorescence excitation–emission matrices (EEMs) were collected on a spectrofluorometer (F4600 Hitachi), forming a three-way array (sample × emission × excitation) for parallel factor analysis (PARAFAC) in MATLAB with the drEEM toolbox (Murphy et al., 2013).

Table 1
Soil characteristics of the Ah horizons (5–15 cm) at Nahuelbuta National Park (NNP) (37°47′S, 72°12′W), Conguillio National Park (CONP) (38°40′S, 71°39′W), Alerce Costero National Park (ACNP) (40°22′S 73°38′W), and Puyehue National Park (PNP) (40°47′ S, 72°12′ W) (Merino et al., 2021).

Site	Soil Order and origin[a]	Texture[b]	Elevation	MAT[c]	MAP[d]	pH	Fe total	CEC[e]	$\delta^{13}C$ (DOC)	$\delta^{13}C$ (SOC)
			ma.s.l.	°C	mm		g kg^{-1}	$cmol_{(+)}$ kg^{-1}	(‰)	
NNP	Inceptisol (granitoid)	SiCL	1.379	13.3	>1.500	3.6	10.4	11.8	−28.0 ± 0.2	−27.2 ± 0.2
CONP	Andisol (volcanic ash)	SL	1.400	10.5	>2.500	5.5	8.6	6.3	−27.4 ± 0.3	−26.5 ± 0.2
ACNP	Ultisol (methamorphic)	CL	1.048	9.5	>4.000	4.5	11.8	19.7	−28.3 ± 0.1	−27.4 ± 0.3
PNP	Andisol (volcanic ash)	SCL	920	9.2	>5.000	5.1	8.4	5.3	−28.1 ± 0.2	−27.3 ± 0.1

[a] Soil Survey Staff (2014).
[b] Texture: SiCL = Silty clay loam; SL = Sandy loam; CL = Clay loam; SCL = Sandy clay loam.
[c] MAT: Mean annual temperature.
[d] MAP: Mean annual precipitation.
[e] Cation exchange capacity.

2.4. Anoxic incubation and controlled re-oxygenation

Ten grams of fresh soil was incubated in gas-tight vials and purged with high-purity N_2 (99.9 %) for 7–14 days at room temperature in the dark. This step allowed accumulation of Fe(II) and reduced DOC (Hall and Silver, 2015). Incubations were performed in quadruplicate (n = 4) for each soil × treatment. Air (21 % O_2) was then introduced in a controlled manner. Redox potential (Eh) was tracked by microelectrodes, and dissolved O_2 was measured with optical sensors (PreSens OXY-1). To test ecological relevance, we applied a four-level H_2O_2 dose-response scheme (5, 30, 100, and 300 μM). The 5 μM level matches hotspot maxima reported for humid forest porewater, whereas 30–300 μM accelerate kinetics and allow a rate constant to be extrapolated to 1 μM (see dose-response results).

2.5. Soil porewater collection (rhizon)

Rhizon samplers (0.15 μm pore size, 5 cm porous length; Rhizosphere Research Products, The Netherlands) were inserted vertically into the 0–10 cm layer of saturated soil. A high vacuum (−1000 kPa) was applied with a sealed pump system connected to 12 mL vials, ensuring extraction from micropores under minimal aeration. This tension exceeded gravitational drainage, targeting anoxic microzones. Nine replicates were collected per site. Each porewater sample was weighed to determine volume, then subdivided: 2 mL were used immediately for pH measurement (glass electrode), and the remainder was acidified to pH < 2 (final HCl ~1 %, v/v) to prevent iron precipitation or speciation changes. Samples were sealed to exclude oxygen and transported at ~5 °C for chemical analysis (Seeberg-Elverfeldt et al., 2005; Gao et al., 2024).

2.6. Fe(II), total Fe, and electron-donating capacity (EDC)

Fe(II) was extracted by shaking 0.1 g soil with 0.5 M HCl. A 100 μL aliquot of the extract was mixed with ferrozine reagent (6.5 M ammonium acetate plus 1 g ferrozine) and measured at 562 nm (Stookey, 1970). To determine total Fe, 100 mg soil was treated with 0.9 mL of 0.28 M hydroxylamine hydrochloride (2 %) and 1 mL of 0.28 M HCl. The difference between total Fe and Fe(II) gave Fe(III). Standards were prepared with ferrous ethylenediammonium sulfate in 0.5 M HCl (Merino et al., 2020b). Filtered (0.2 μm) porewater was analyzed with an electrochemical workstation (CHI660E, Shanghai, China) equipped with a three-electrode cell (Ag/AgCl reference, Pt counter, glassy C working). A phosphate buffer (0.2 M, pH 7.0) and KCl (0.2 M) served as the electrolyte. After N_2 purging (~5 min), 1 mL of oxidant (ABTS) was added, followed by 1 mL of sample (Page et al., 2013a). The integrated oxidation current (A_p, in coulombs) was converted to EDC (mol e^- g^{-1} C) using:

$$EDC = \frac{A_p}{NA \times e \times MC}$$

where NA is Avogadro's constant (6.02×10^{-23} mol^{-1}), e is the electron charge (1.6×10^{-19} C), and MC is the mass of C in the reaction (5×10^{-5} g). Procedural blanks (n = 5) remained below the detection limit (0.02 mmol e^- g^{-1} C), and spike-recovery tests with Fe(II) standards (5–50 μM) yielded 97 ± 4 % recovery. This value reflects the electron donation from Fe(II) and redox-active DOM.

2.7. Hydrogen peroxide (H_2O_2) and hydroxyl radicals (•OH)

H_2O_2 was measured by iodometric titration (Velikova et al., 2000). •OH was detected with terephthalic acid (TPA), which forms a fluorescent product (hydroxy-terephthalate) upon oxidation (Klüpfel et al., 2014). After 24 h of dark incubation, the reaction mixture was filtered (0.22 μm) and measured fluorescence (λ_ex = 310 nm, λ_em = 425 nm). Calibration with external 2-hydroxyterephthalate standards yielded a detection limit of 0.8 nM •OH; replicate precision was ±0.3 nM (n = 6).

2.8. Abiotic CO_2 production from DOC

Anoxic porewater was split into two microbial-inhibition treatments: (i) filter sterilization (0.2 μm) and (ii) addition of 0.1 % NaN_3. A 48 h pre-test confirmed that NaN_3 (0.1 %) suppressed microbial respiration by 96 ± 3 % while leaving H_2O_2 decay unchanged. Each treated sample (15 mL) was placed in a sterile 20 mL serum vial, leaving ~5 mL headspace. The headspace was purged with high-purity N_2 (99.9 %), then the vial was sealed with a butyl stopper and crimp-capped. H_2O_2 (5–300 μM) was injected through the stopper. Samples were incubated for 24 h at room temperature in the dark. Controls without H_2O_2 evaluated baseline CO_2 release, and additional unsterilized vials served as biotic controls. After incubation, a gas-tight syringe sampled the headspace for CO_2 quantification on a gas chromatograph (Thermo Fisher Scientific™, Austin, TX, USA). The difference in CO_2 between H_2O_2-treated and control vials indicated abiotic DOC oxidation (Liu et al., 2019; Jofré-Fernández et al., 2023). The origin of the CO_2 was traced using the natural $\delta^{13}C$ difference between DOC and bulk SOM, measured by isotope ratio mass spectrometer (IRMS) (Thermo Fisher Scientific, Bremen, Germany) (Page et al., 2013b). For each H_2O_2 concentration, the first-order rate constant for CO_2 accumulation was estimated, and plotting these constants against the initial [H_2O_2] enabled interpolation to 1 μM.

2.9. Statistical analyses

A one-way ANOVA followed by Tukey's post hoc test ($p < 0.05$) compared CO_2 production across soil types and H_2O_2 concentrations. A Shapiro–Wilk test verified normal data distribution, and Levene's test checked homoscedasticity. Linear regressions were fitted to examine relationships among Fe(II), EDC, H_2O_2, •OH, and CO_2. To test whether the dose–response slope (rate constant vs. [H_2O_2]) differed among soils, we applied extra-sum-of-squares F-tests ($p < 0.05$). An ANCOVA

assessed whether slopes differed among soils in each relationship ($p < 0.05$). All calculations were performed in RStudio (version 4.3.1).

3. Results

3.1. Pore-size distribution

All four soils are dominated by micropores ranging from 2.5 to 10 μm. Sandy clay loam (SCL) contains more patches near ~8–10 μm, while silty clay loam (SiCL) shows fewer pores above ~7 μm (Fig. 1A). The density plot indicates that SCL distribution extends further toward ~9 μm, whereas SiCL curve peaks around 4–5 μm and declines more sharply beyond 7 μm. Approximately 15 % of SCL pores exceed 7 μm, compared with under 5 % in SiCL (Fig. 1B). Across soils, the volume-weighted fraction of pores <10 μm ranged from 22 ± 2 % (SiCL) to 37 ± 3 % (SCL) and correlated with both initial Fe(II) stocks ($R^2 = 0.82$, $p < 0.01$) and the •OH formed during re-oxygenation ($R^2 = 0.79$, $p < 0.01$; see Supplementary Table S1).

3.2. Initial conditions of soil porewater

SCL contained the highest DOC concentration (~6 mg L^{-1}) and Fe(II) (~35 μM), while SiCL had the lowest (~3.5 mg L^{-1} and ~15 μM, respectively). pH ranged from ~3.7 to ~5.3, with electron-donating capacity (EDC) at 0.18–0.33 μmol e^- L^{-1}. H_2O_2 and •OH were also higher in SCL, whereas SiCL had the lowest values for both. CL and SL presented intermediate values across these parameters (Table 2).

3.3. Redox changes and formation of reactive species

Under re-oxygenation, soils with elevated Fe(II) (e.g., SCL) showed a sharper Fe(II) drop (from ~35 to <10 μM) and a stronger rise in Eh (from ~200 to ~320 mV) (Fig. 2A and B). Dissolved oxygen in these soils increased by ~20–25 μM, whereas soils with lower or moderate Fe (II) (SiCL, CL, SL) reached ~15–20 μM (Fig. 2C). Hydrogen peroxide peaked at ~2–3 μM in SCL but remained around 0.2–1 μM elsewhere (Fig. 2D). Hydroxyl radicals likewise approached ~20–25 nM in soils with abundant Fe(II) and remained near 10–12 nM where Fe(II) was lower (Fig. 2E).

3.4. Abiotic CO_2 production

After 24 h with 100 μM H_2O_2, SCL displayed a ~20 % increase in CO_2, CL reached ~15 %, SL ~10 %, and SiCL ~5 % (Fig. 3). These increments represent net abiotic CO_2 formed beyond the baseline (i.e., vials without H_2O_2). The $\delta^{13}C$ of this extra CO_2 (−26.7 ± 0.12 ‰ in SCL) differed from the bulk SOC end-member (−27.2 ± 0.18 ‰) by 2.9–4.1 σ, confirming a DOC origin within the analytical uncertainty (*t*-test, $p < 0.01$).

3.5. H_2O_2 dose–response and isotopic measurements

At 100 μM H_2O_2, soils with higher Fe(II) (e.g., SCL or CL) showed net CO_2 increments of up to ~20 %, whereas those with lower Fe(II) (e.g., SL or SiCL) reached only ~10 % or less (Fig. 4A). At 300 μM H_2O_2, SCL approached ~25 %, while SiCL remained <5 % (Fig. 4B). The $\delta^{13}C$ of the released CO_2 ranged from ~−26.7 ‰ (SCL) to ~ −24.4 ‰ (SL), matching the labeled DOC source (Fig. 4C). The first-order rate constants for abiotic CO_2 accumulation ($k_{abiotic}$) increased linearly with the initial H_2O_2 concentration ($R^2 = 0.94$) (Table S2). The pooled slope was 1.7×10^{-3} h^{-1} μM^{-1} ± 0.2×10^{-3} (95 % CI), and the intercept 2.1×10^{-3} h^{-1}. Extrapolation to 1 μM H_2O_2 predicts an abiotic contribution of 1–2 % of the total soil CO_2, consistent with field hotspot estimates. Extra sum-of-squares F-tests showed no slope differences among soils ($p = 0.31$).

3.6. Relationships among •OH, EDC, Fe(II), and CO_2

Hydroxyl-radical formation (Δ•OH, net change from initial to final) correlated linearly with ΔCO_2 (net CO_2 release) in each soil (Fig. 5A). SCL had a steeper slope than the other soils (~5 nM increase in •OH per unit of CO_2 rise). Electron-donating capacity (ΔEDC) also aligned with ΔCO_2, indicating stronger electron transfer in SCL than in SiCL (Fig. 5B). Changes in Fe(II) (ΔFe(II)) were associated with Δ•OH, reflecting that Fe(II) depletion (up to ~10 μM h^{-1} in SCL) accompanied higher •OH formation rates (Fig. 5C). The slopes for Δ•OH versus ΔCO_2 (Panel A) differed across soils ($p = 0.0044$), with SCL showing a steeper slope than the others. The slopes for ΔEDC versus ΔCO_2 (Panel B) did not differ ($p = 0.55$), implying a similar slope among the soils. The slopes for ΔFe(II)

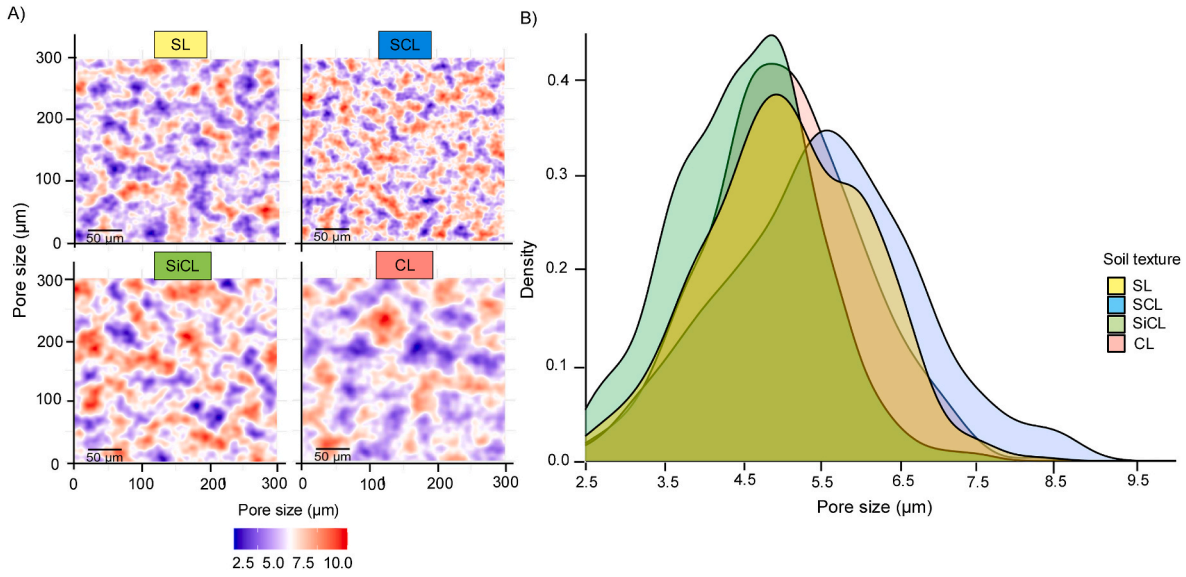

Fig. 1. (A) Micro-CT (micro-computed tomography) pore diameter maps (2.5–10.0 μm) in four soils, arranged left to right by increasing clay content: sandy loam (SL), sandy clay loam (SCL), silty clay loam (SiCL), and clay loam (CL). Red areas indicate ~10.0 μm pores, blue areas ~2.5 μm pores. Scale bar: 50 μm; (B) Overlaid density plots of pore diameters from the same soils. Each curve shows the distribution of pore sizes, color-coded by soil type, within the 2.5–10.0 μm range. Note that because only small aggregates (>300 μm) were scanned by μCT, the pores >10 μm are not presented. (For interpretation of the references to color in this figure legend, the reader is referred to the Web version of this article.)

Table 2
Initial porewater conditions (mean ± standard error, n = 4) and content of DOC, Fe(II) and oxygen radicals in four soils, arranged left to right by increasing clay content: sandy loam (SL), sandy clay loam (SCL), silty clay loam (SiCL), and clay loam (CL).

Soil	DOC[a] (mg $L^{-}1$)	Fe(II)[b](μM)	Fe dissolved[c] (μM)	pH	EDC[d] (μmol e− $L^{-}1$)	H_2O_2[e] (μM)	•OH[f] (nM)
SL	4.0 ± 0.3	20 ± 1	34 ± 2	5.3 ± 0.03	0.22 ± 0.01	0.4 ± 0.05	8 ± 2
SCL	6.2 ± 0.3	35 ± 2	42 ± 2	5.0 ± 0.02	0.33 ± 0.02	0.9 ± 0.10	20 ± 5
SiCL	3.5 ± 0.2	15 ± 1	30 ± 2	3.7 ± 0.05	0.18 ± 0.01	0.2 ± 0.02	5 ± 1
CL	5.0 ± 0.4	28 ± 1	38 ± 2	4.3 ± 0.04	0.27 ± 0.01	0.6 ± 0.05	12 ± 3

[a] DOC is dissolved organic carbon (mg L^{-1}).
[b] Fe(II) (μM) is ferrous iron in soil solution.
[c] Fe dissolved (μM) is total dissolved iron.
[d] EDC is electron-donating capacity (μmol e^{-} L^{-1}).
[e] H_2O_2 (μM) is hydrogen peroxide; and.
[f] •OH (nM) is hydroxyl radical.

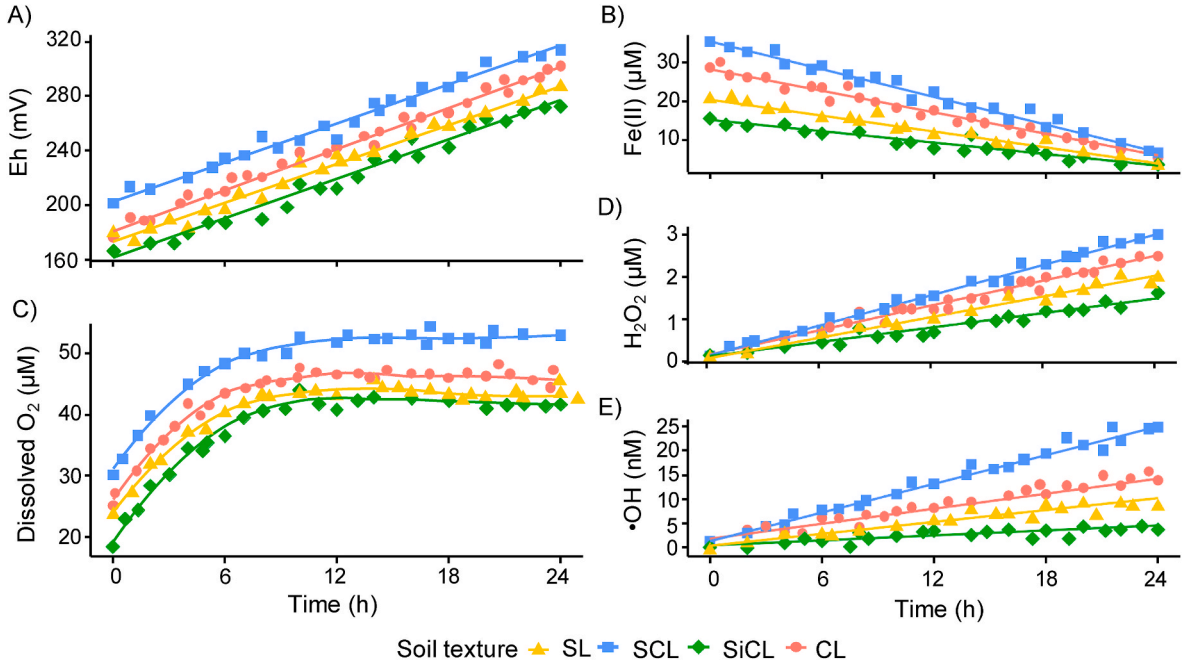

Fig. 2. (A) Redox potential (Eh, mV), (B) Fe(II) (μM), (C) O_2 (μM), (D) H_2O_2 (μM), and (E) •OH (nM) during 24 h of re-oxygenation in four soils, arranged left to right by increasing clay content: sandy loam (SL), sandy clay loam (SCL), silty clay loam (SiCL), and clay loam (CL). Each symbol is a mean value (n = 30), and lines connect time points. Eh is in millivolts. Abbreviations: Fe(II) ferrous iron, O_2 dissolved oxygen, H_2O_2 hydrogen peroxide, •OH hydroxyl radicals.

versus Δ•OH (Panel C) also did not differ ($p = 0.15$). The four soils were pooled (n = 64), Δ•OH explained 86 % of the variance in ΔCO_2, while the microporosity-to-Fe(II) ratio explained 78 % of the variance in Δ•OH (Table S1).

3.7. DOC composition and aromaticity

SCL contained a larger portion of aromatic-like compounds (~65–75 %) and had higher $SUVA_{254}$ (~4.0 L mg^{-1} m^{-1}) than the other soils (Fig. 6). In contrast, SiCL included more low-molecular-weight compounds (~30–35 %) and had a lower $SUVA_{254}$ (~3.0 L mg^{-1} m^{-1}). CL and SL presented intermediate proportions of these compounds. These differences in aromaticity align with the elevated radical production and CO_2 release in SCL.

4. Discussion

4.1. Fe(II) as the main electron donor for •OH

SCL, with ~35 μM Fe(II), displayed the largest increase in •OH after re-oxygenation (Fig. 2B and E), whereas SiCL, containing ~15 μM Fe(II), generated fewer radicals. This contrast indicates that Fe(II) availability governs radical formation more strongly than potential electron transfer by low-molecular-weight compounds of DOC (Fig. 5C). In SCL, Fe(II) declined sharply from ~35 to <10 μM, coinciding with higher H_2O_2 and •OH, which points to iron oxidation as the main driver of dark Fenton-type processes.

These findings confirm that Fe(II) surpasses DOC as the main electron donor under fluctuating redox conditions, at least if sufficiently available. Low-molecular-weight DOC donates electrons when Fe(II) is scarce (Keller et al., 2009; Zhao et al., 2021). By contrast, Zhang et al. (2022) reported that high C/Fe ratios favor electron transfer from humic substances. Similarly, Yu et al. (2022) found that in soils or sediments with elevated SOC/Fe(II) ratios, reduced SOM can even dominate •OH production. However, in our soils, the moderate DOC levels apparently allowed Fe(II) to govern radical generation. As Fe(II) availability rises, the radical flux increases once O_2 enters micropores (Fig. 2C–E). This aligns with previous work on iron-rich soils under transient oxic–anoxic conditions (Mollhagen et al., 2021; Xu et al., 2024). Experiments in other humid forest soils, where Fe(II) and ligninolytic enzymes co-occur, further support iron-driven oxidation (Merino et al., 2020a). Overall, soils with high Fe(II) concentrations showed a steep drop in Fe(II) levels upon oxygen influx and produced more H_2O_2 and •OH (Fig. 2D and E), confirming that iron oxidation dominates radical formation during short

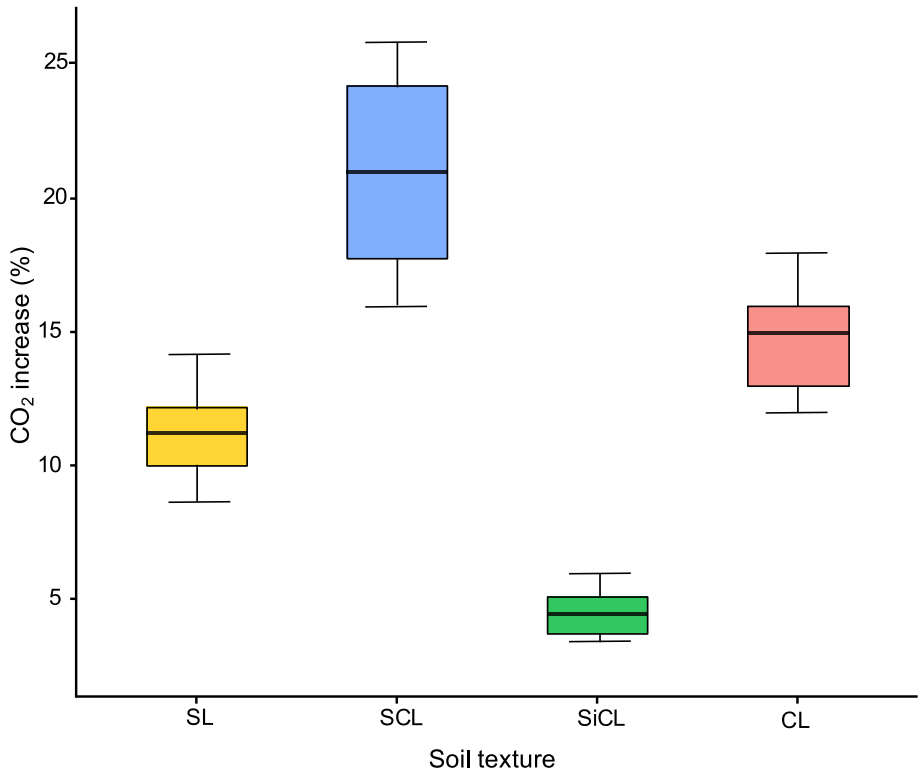

Fig. 3. Net CO_2 increase (%) relative to control without H_2O_2 after 24 h of incubation with 100 μM H_2O_2 in four soils, arranged left to right by increasing clay content: sandy loam (SL), sandy clay loam (SCL), silty clay loam (SiCL), and clay loam (CL). Each box spans the interquartile range (25^{th}–75^{th} percentile). Whiskers extend to ±1.5 × IQR; the horizontal line in each box shows the median (n = 30).

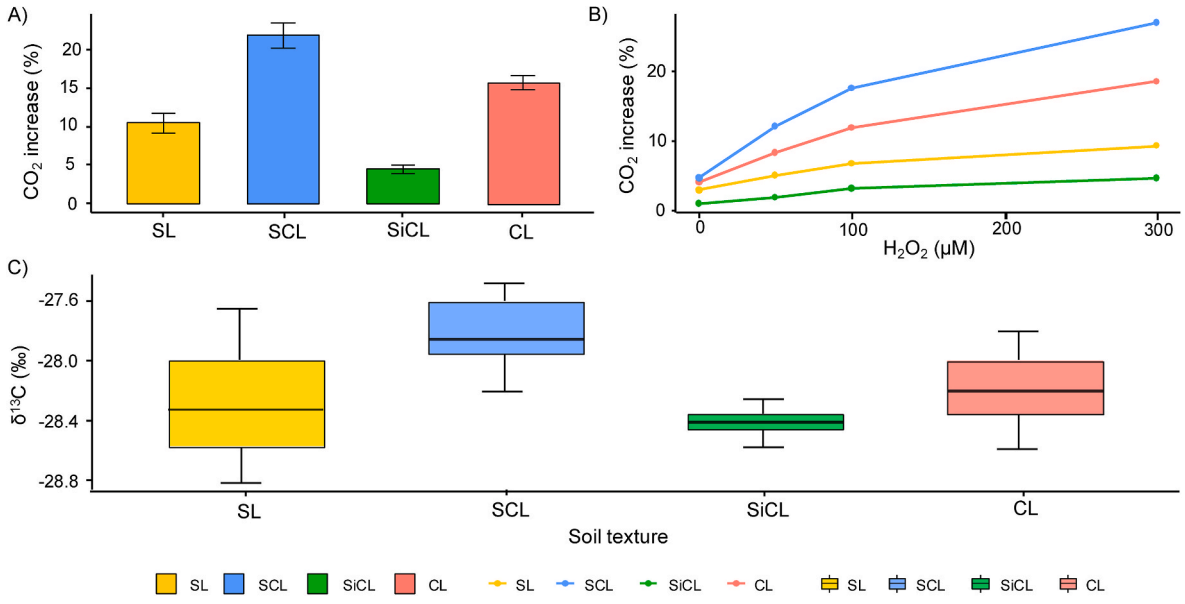

Fig. 4. (A) Net CO_2 increase (%) relative to control without H_2O_2 measured after 24 h with 100 μM H_2O_2 in four soils, shown left to right by increasing clay content: sandy loam (SL), sandy clay loam (SCL), silty clay loam (SiCL), and clay loam (CL). Bars: mean values; error bars: ± standard error (n = 30). (B) CO_2 increase (%) at 5–300 μM H_2O_2 for the same soils. Each symbol corresponds to the mean of four replicate measurements. (C) $\delta^{13}C$ of CO_2 (‰) measured from DOC oxidation. Boxes: the interquartile range (25^{th}–75^{th} percentile); horizontal line within each box the median; circles: replicate data points. Whiskers extend to 1.5 × IQR.

anoxic–oxic pulses.

4.2. Magnitude of abiotic CO_2 from DOC oxidation

SCL released ~20 % more CO_2 at 100 μM H_2O_2 than the other soils due to its high Fe(II) (~35 μM) and DOC (~6 mg L^{-1}) content (Figs. 3 and 4A). SiCL released only ~5 % extra CO_2, whereas CL and SL ranged between 5 and 15 %. At 300 μM H_2O_2, SCL approached ~25 % additional CO_2 (Fig. 4B). These CO_2 increases over the controls (without H_2O_2 addition) indicate that Fe(II) and labile DOC jointly drive radical-mediated oxidation, because soils with the highest Fe(II) and most aromatic DOC (SCL) released the largest fraction of abiotic CO_2.

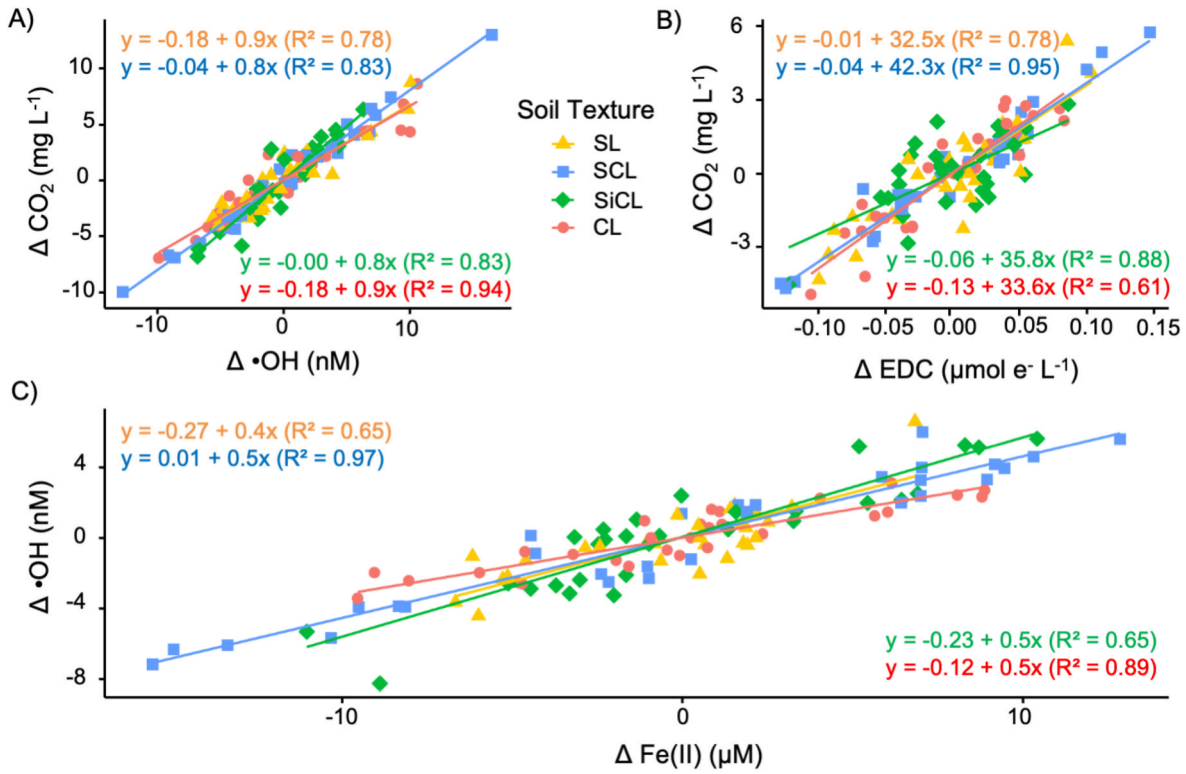

Fig. 5. Regressions between (A) net change in •OH (Δ•OH, nM) vs. net change in CO_2 (ΔCO_2 mg L^{-1}), (B) net change in electron-donating capacity (ΔEDC, μmol e^- L^{-1}) vs. ΔCO_2, and (C) net change in Fe(II) (ΔFe(II), μM) vs. Δ•OH for four soils arranged left to right by increasing clay content: sandy loam (SL), sandy clay loam (SCL), silty clay loam (SiCL), and clay loam (CL). Lines are linear regressions fitted separately for each soil.

Although $\delta^{13}C$(DOC) and $\delta^{13}C$(SOC) differ by only ~0.8–1.0 ‰ (Table 1) a slight but consistent gap typical of C_3 soils (Werth and Kuzyakov, 2010) it confirms that the dissolved fraction, but not the solid phase, dominates the extra CO_2 formed under Fenton-type conditions. The excess CO_2 averaged −26.7 ± 0.12 ‰, whereas bulk SOC was −27.2 ± 0.18 ‰; this 0.5 ‰ offset equals 2.9–4.1 analytical σ (*t*-test, $p < 0.01$), thus exceeding the measurement uncertainty. Because DOC contains much more labile compounds, it oxidizes faster, matching the short-term pulse of hydroxyl radicals and Fe(II) depletion (Fig. 5C). These patterns confirm that aromatic-rich DOC pools together with Fe(II) inside pores <10 μm, a combination that amplifies •OH bursts when O_2 enters; the micropore fraction explains 82 % of the initial Fe(II) stock and 79 % of •OH production (Table S1).

Inhibition of microbial respiration by NaN_3 and removal of microbial cells by filtration at 0.2 μm exclude respiration from living biomass. The rapid correlation between Fe(II) depletion, H_2O_2, and CO_2 release within ~24 h suggests an abiotic pathway. A purely microbial mechanism would likely require longer activation times (Hassi et al., 2023), reinforcing that most of the additional CO_2 originated from chemical oxidation rather than microbial respiration.

The dark Fenton-type processes can account for ~15–25 % of total soil respiration under transient anoxia–oxia (Merino et al., 2020a, 2020b, 2021). Moreover, ~15–25 % of CO_2 may arise from hydroxyl radicals in sandy soils (Liu et al., 2023b). Iron-bearing solution experiments also yielded ~5–20 % abiotic DOC oxidation (Chen et al., 2020; Patzner et al., 2020). Soils with lower Fe(II) content or lower DOC aromaticity have smaller fluxes than soils rich in both Fe(II) and aromatic DOC (Kramer et al., 2012; Li et al., 2022). Comparable ROS-driven incubations report abiotic contributions of 6–12 % in Chinese paddy soils (Jeewani et al., 2021), 16–26 % in restored sandy forest soils (Liu et al., 2023a) and 9–17 % after gallic-acid-induced Fenton reactions in temperate grassland soils (Halvorson et al., 2025); thus, our 5–25 % range sits at—or above—the upper end of published values. Overall, these results indicate that radical-driven DOC oxidation can contribute ~5–25 % of additional CO_2 adding to the microbial respiration in humid forest soils. This reinforces the hypothesis that non-biological pathways strongly expand total C losses.

Notably, sandy soils (SL, SCL) in this study coincide with volcanic origin, while finer soils (SiCL, CL) derive from granite or metamorphic substrates. This overlap of texture and lithology means microporosity depends on both, so each soil's CO_2 production reflects a combined influence of Fe(II), pore structure, and DOC characteristics, rather than any single factor alone. Extrapolating the $k_{abiotic}$–[H_2O_2] regression to 1 μM (Table S2) yields only a 1–2 % increase in CO_2, in line with in situ microsensor records of 0.5–1.2 μM H_2O_2 in humid-forest porewater (van Erk et al., 2023).

Fig. 7 provides a conceptual overview of these results, illustrating how soils with higher Fe(II) availability, microporosity, and aromatic DOC (especially SCL) intensively generate radicals leading to high abiotic CO_2 production. By contrast, soils with lower iron and less aromatic DOC (here SiCL) show minimal radical-driven oxidation (5–10 % of abiotic CO_2 of total CO_2). Intermediate conditions in SL and CL soils lead to moderate abiotic CO_2 fluxes (~10 % and ~15 % of total CO_2, respectively). This concept integrates the Fe(II) availability, microporosity, and DOC aromaticity for radical generation, rather than the soil texture alone. The SCL provides an example of high Fe(II) and abundant micropores, yet SiCL, also fine-textured, has less Fe(II) and produces fewer radicals. Hence, multiple factors, not solely texture, control the magnitude of abiotic CO_2 release.

4.3. *Influence of microporosity and redox fluctuations on abiotic CO_2 emissions*

All soils contained micropores of 2.5–10 μm that limit oxygen diffusion, thereby stabilizing Fe(II) when pores remain water-filled (Totsche et al., 2018). Under re-oxygenation, SCL reached ~20–25 μM

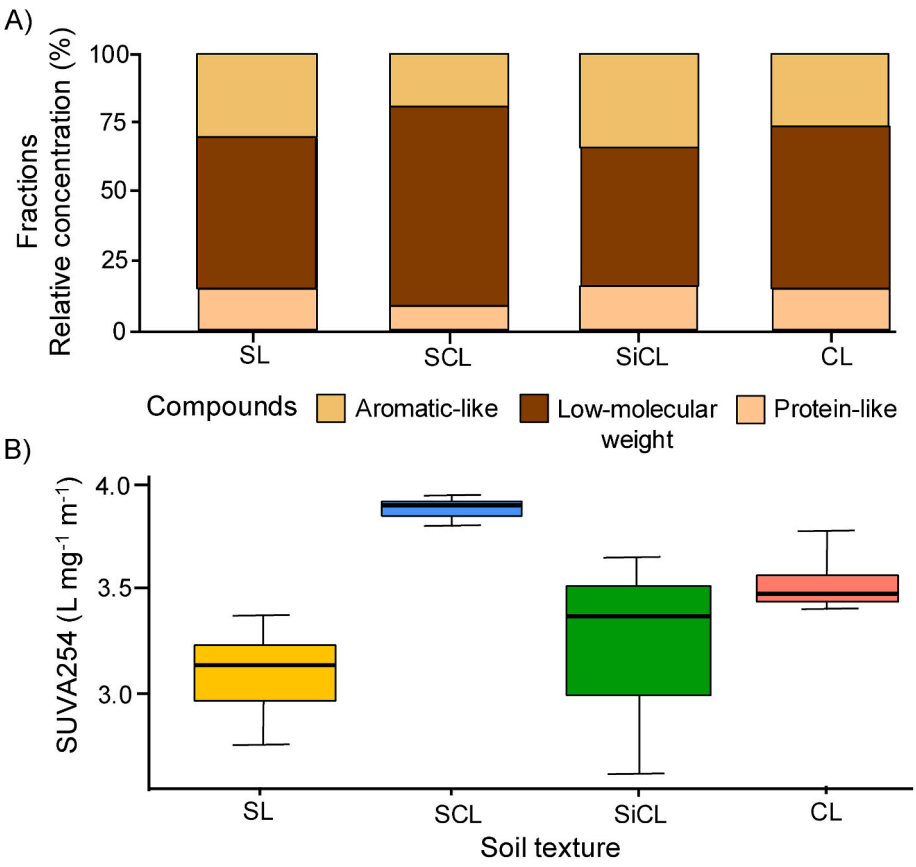

Fig. 6. (A) Relative content of aromatic-like, low-molecular-weight, and protein-like DOC fractions in four soils, arranged left to right by increasing clay content: sandy loam (SL), sandy clay loam (SCL), silty clay loam (SiCL), and clay loam (CL). (parallel factor analysis). (B) $SUVA_{254}$ (L mg^{-1} m^{-1}) for the same soils. Boxplots display medians and quartiles (n = 9).

dissolved O_2, whereas CL, SL, and SiCL approached ~15–20 μM O_2 (Fig. 2C). The partial penetration of O_2 triggered H_2O_2 formation and radical production (Fig. 2D), especially in micropores <10 μm, which repeatedly shift between previous anoxic to new oxic states (Keiluweit et al., 2018). Yudina et al. (2022) noted that microaggregates create complex pore networks, raising water retention and sustaining local anoxia until air re-enters during drainage or other shifts in soil moisture. Large pores (>50 μm) permit faster O_2 diffusion and thus less anoxia (Schlüter et al., 2018), but these soils feature a high proportion of smaller pores, which maintain Fe(II) for short periods until rainfall or partial drying drives oxygen deeper into the aggregates (Li et al., 2020; Slimani et al., 2023).

Consequently, transient anoxia persists in many micropores, promoting Fe(II) accumulation and fueling radical-mediated DOC oxidation upon brief oxygen pulses. This mechanism underscores how microaggregation and pore-size distribution amplify Fenton-type processes in humid forest soils, where water saturation and airflow fluctuate on daily to weekly timescales.

4.4. Implications for C cycling in humid forest soils

SCL contained ~65–75 % aromatic-rich DOC with a $SUVA_{254}$ near 4.0 L mg^{-1} m^{-1} (Fig. 6), which enables electron exchange with Fe(II) and boosts radical formation (Cory and McKnight, 2005; Derbalah et al., 2020). This combined effect of elevated Fe(II) (~35 μM) and aromatic DOC yielded ~20 % additional CO_2 from radical-mediated oxidation at 100 μM H_2O_2 (Fig. 3). Modeling suggests that dark Fenton-type reactions intensify when rainfall patterns fluctuate, creating short anoxic–oxic intervals (Yu et al., 2021; Yu and Kuzyakov, 2021). These brief waterlogged phases allow Fe(II) to accumulate without displacing microbial respiration, thus adding a chemical oxidation pathway on top of the biological baseline (LaCroix et al., 2019). Soils with high Fe(II) availability and aromatic DOC release more CO_2 once oxygen re-enters, confirming that Fe(II)-driven radical formation under fluctuating redox conditions raises carbon losses in soils of humid forest ecosystems. Incorporating $k_{abiotic}$ into process-based soil carbon models, such as MIMICS or SOCRATES, would lower the effective microbial respiration parameter by 5–25 % during redox oscillations, bringing simulated fluxes into closer agreement with eddy covariance residuals from humid forests (Bond-Lamberty et al., 2020).

Our 24 h static-core incubations and external H_2O_2 additions accelerated radical formation but may have overestimated field rates; therefore, we treated 5 μM as an upper natural bound. Future studies that combine ROS microsensors, microdialysis, and in situ ^{13}C tracing (Hall and Silver, 2013; van Erk et al., 2023) should quantify $k_{abiotic}$ under ambient H_2O_2 and realistic hydrodynamics, thereby refining the abiotic term before it is incorporated into global soil-carbon models.

5. Conclusions

Although micropores of 2.5–10 μm maintain anoxic conditions and consequently the Fe(II) concentration, the radical production depends on factors such as Fe(II) availability and DOC aromaticity. For instance, SiCL had fine pores yet released the least CO_2. Overall, these findings confirm that transient anoxia raises abiotic DOC oxidation and adds a non-biological CO_2 component to soil fluxes. Accordingly, carbon losses in fluctuating redox environments should not be attributed solely to microbial processes. Our results also demonstrate that hydroxyl radical (•OH) formation during anoxic–oxic transitions is a key pathway for abiotic CO_2 release in four humid forest soils. Natural $\delta^{13}C$ signatures

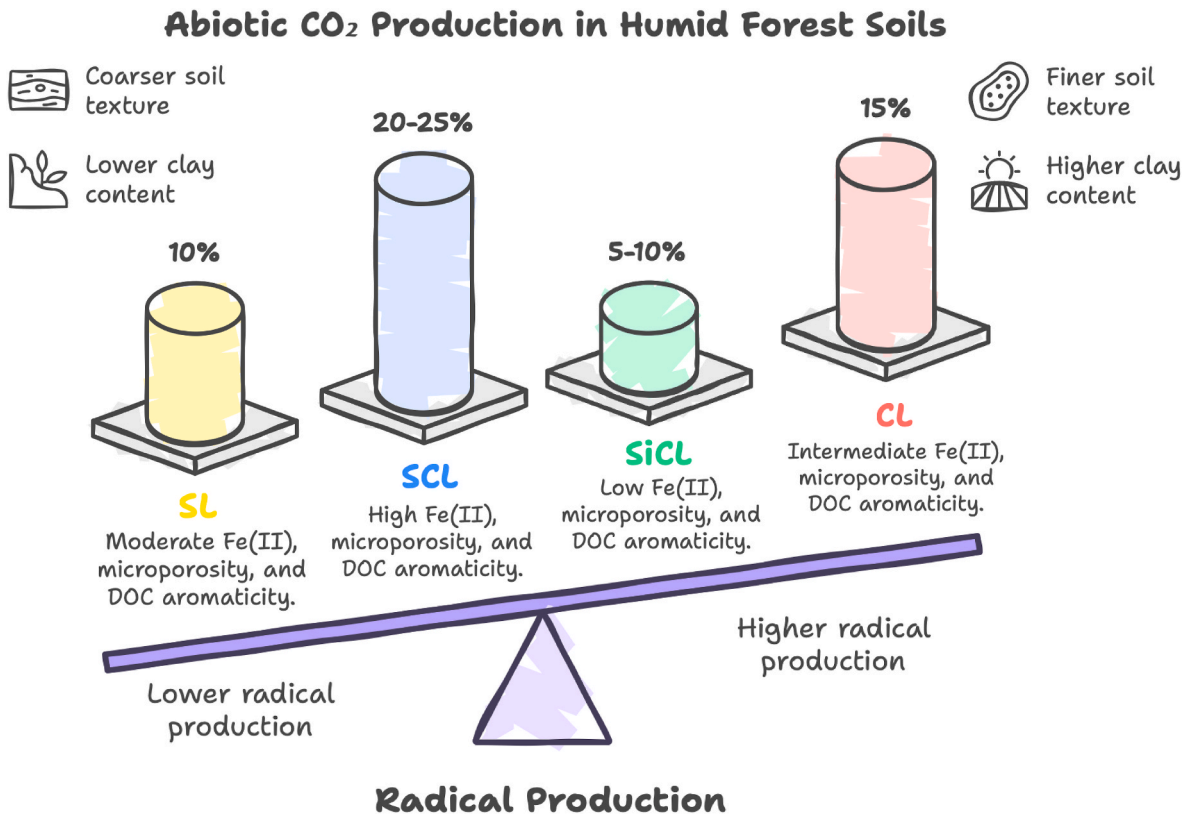

Fig. 7. Conceptual diagram showing oxygen radical-driven CO_2 production in four humid forest soils.

confirmed that dissolved organic carbon (DOC), rather than bulk SOM, supplies most of the substrate for radical driven oxidation. Moreover, Fe (II) (~15–35 μM) surpassed DOC as the primary electron donor for dark Fenton-type reactions, oxidizing ~5–20 % of DOC to CO_2 over hours to days. Recognizing Fe(II) driven radical generation as a major carbon-loss mechanism highlights the importance of non-biological processes under dynamic redox conditions.

CRediT authorship contribution statement

Carolina Merino: Conceptualization, Data curation, Formal analysis, Funding acquisition, Methodology, Writing – original draft, Writing – review & editing. **Ignacio Jofré:** Methodology, Writing – original draft. **Francisco Nájera:** Methodology, Writing – original draft. **Francisco Matus:** Formal analysis, Writing – original draft. **Felipe Aburto:** Conceptualization, Data curation. **José Dörner:** Conceptualization, Data curation, Formal analysis. **Rafael Rubilar:** Conceptualization, Writing – original draft. **Michaela A. Dippold:** Conceptualization, Data curation, Formal analysis, Writing – original draft, Writing – review & editing. **Yakov Kuzyakov:** Conceptualization, Data curation, Formal analysis, Validation, Writing – original draft, Writing – review & editing.

Declaration of competing interest

The authors declare that they have no known competing financial interests or personal relationships that could have appeared to influence the work reported in this paper.

Acknowledgements

This work was financed by ANID-FONDECYT Regular Project N°1220716. ANID-FONDECYT Postdoctoral Project N° 3230428. Open access of this article was funded from the Ministry of Education, Science and Sports of the Republic of Lithuania and Research Council of Lithuania (LMTLT) under the Program 'University Excellence Initiative' Project 'Development of the Bioeconomy Research Center of Excellence' (BioTEC), agreement No S-A-UEI-23-14.

Appendix A. Supplementary data

Supplementary data to this article can be found online at https://doi.org/10.1016/j.soilbio.2025.109951.

References

Ayeni, T.T., Iwamoto, Y., Takeda, K., Sakugawa, H., Mostofa, K.M.G., 2022. Optical properties of dissolved organic matter in Japanese Rivers and contributions to photoformation of reactive oxygen species. Science of The Total Environment 826, 153671.

Barcellos, D., Cyle, K.T., Thompson, A., 2018. Faster redox fluctuations can lead to higher iron reduction rates in humid forest soils. Biogeochemistry 137, 367–378.

Barcellos, D., Pérez Castro, S., Campbell, A., Kimbrel, J.A., Blazewicz, S.J., Wollard, J., Pett-Ridge, J., Thompson, A., 2025. Duration of O2 exposure determines dominance of FeII vs CH4 production in tropical Forest soils. Environmental Science & Technology.

Bond-Lamberty, B., Christianson, D.S., Malhotra, A., Pennington, S.C., Sihi, D., AghaKouchak, A., Anjileli, H., Altaf Arain, M., Armesto, J.J., Ashraf, S., Ataka, M., Baldocchi, D., Andrew Black, T., Buchmann, N., Carbone, M.S., Chang, S.-C., Crill, P., Curtis, P.S., Davidson, E.A., Desai, A.R., Drake, J.E., El-Madany, T.S., Gavazzi, M., Görres, C.-M., Gough, C.M., Goulden, M., Gregg, J., Gutiérrez del Arroyo, O., He, J.-S., Hirano, T., Hopple, A., Hughes, H., Järveoja, J., Jassal, R., Jian, J., Kan, H., Kaye, J., Kominami, Y., Liang, N., Lipson, D., Macdonald, C.A., Maseyk, K., Mathes, K., Mauritz, M., Mayes, M.A., McNulty, S., Miao, G., Migliavacca, M., Miller, S., Miniat, C.F., Nietz, J.G., Nilsson, M.B., Noormets, A., Norouzi, H., O'Connell, C.S., Osborne, B., Oyonarte, C., Pang, Z., Peichl, M., Pendall, E., Perez-Quezada, J.F., Phillips, C.L., Phillips, R.P., Raich, J.W., Renchon, A.A., Ruehr, N.K., Sánchez-Cañete, E.P., Saunders, M., Savage, K.E., Schrumpf, M., Scott, R.L., Seibt, U., Silver, W.L., Sun, W., Szutu, D., Takagi, K., Takagi, M., Teramoto, M., Tjoelker, M.G., Trumbore, S., Ueyama, M., Vargas, R., Varner, R.K., Verfaillie, J., Vogel, C., Wang, J., Winston, G., Wood, T.E., Wu, J., Wutzler, T., Zeng, J., Zha, T., Zhang, Q., Zou, J., 2020. COSORE: a community database for continuous soil respiration and other soil-atmosphere greenhouse gas flux data. Global Change Biology 26, 7268–7283.

Chen, C., Hall, S.J., Coward, E., Thompson, A., 2020. Iron-mediated organic matter decomposition in humid soils can counteract protection. Nature Communications 11, 2255.
Cory, R.M., McKnight, D.M., 2005. Fluorescence spectroscopy reveals ubiquitous presence of oxidized and reduced quinones in dissolved organic matter. Environmental Science & Technology 39, 8142–8149.
Dec, D., Zúniga, F., Thiers, O., Paulino, L., Valle, S., Villagra, V., Tadich, I., Horn, R., Dörner, J., 2017. Water and temperature dynamics of Aquands under different uses in southern Chile. Journal of Soil Science and Plant Nutrition 17, 141–154.
Derbalah, A., Sunday, M., Kato, R., Takeda, K., Sakugawa, H., 2020. Photoformation of reactive oxygen species and their potential to degrade highly toxic carbaryl and methomyl in river water. Chemosphere 244, 125464.
Dörner, J., Dec, D., Thiers, O., Paulino, L., Zúñiga, F., Valle, S., Martínez, O., Horn, R., 2016. Spatial and temporal variability of physical properties of Aquands under different land uses in southern Chile. Soil Use & Management 32, 411–421.
Dörner, J., Huertas, J., Cuevas, J.G., Leiva, C., Paulino, L., Arumí, J.L., 2015. Water content dynamics in a volcanic ash soil slope in southern Chile. Journal of Plant Nutrition and Soil Science 178, 693–702.
Gao, A.-X., Chen, C., Gao, Z.-Y., Zhai, Z.-Q., Wang, P., Zhang, S.-Y., Zhao, F.-J., 2024. Soil redox status governs within-field spatial variation in microbial arsenic methylation and rice straighthead disease. The ISME Journal 18.
Hall, S.J., Silver, W.L., 2013. Iron oxidation stimulates organic matter decomposition in humid tropical forest soils. Global Change Biology 19, 2804–2813.
Hall, S.J., Silver, W.L., 2015. Reducing conditions, reactive metals, and their interactions can explain spatial patterns of surface soil carbon in a humid tropical forest. Biogeochemistry 125, 149–165.
Halvorson, J.J., Jin, V.L., Liebig, M.A., Schmidt, M.A., Hagerman, A.E., Luciano, R., 2025. Rapid formation of abiotic CO2 after adding phenolic gallic acid, to agricultural soils. Agrosystems. Geosciences & Environment 8, e70035.
Hassi, U., Hu, J., Sleutel, S., De Neve, S., 2023. Recovery of soil microbial community structure and activity following partial sterilization with gamma irradiation. Applied Soil Ecology 187, 104839.
Hu, D., Zeng, Q., Zhu, J., He, C., Shi, Q., Dong, H., 2023. Promotion of Humic acid transformation by abiotic and Biotic Fe redox cycling in nontronite. Environmental Science & Technology 57, 19760–19771.
Jeewani, P.H., Van Zwieten, L., Zhu, Z., Ge, T., Guggenberger, G., Luo, Y., Xu, J., 2021. Abiotic and biotic regulation on carbon mineralization and stabilization in paddy soils along iron oxide gradients. Soil Biology and Biochemistry 160, 108312.
Jofré-Fernández, I., Matus-Baeza, F., Merino-Guzmán, C., 2023. White-rot fungi scavenge reactive oxygen species, which drives pH-dependent exo-enzymatic mechanisms and promotes CO(2) efflux. Frontiers in Microbiology 14, 1148750.
Keiluweit, M., Gee, K., Denney, A., Fendorf, S., 2018. Anoxic microsites in upland soils dominantly controlled by clay content. Soil Biology and Biochemistry 118, 42–50.
Keiluweit, M., Wanzek, T., Kleber, M., Nico, P., Fendorf, S., 2017. Anaerobic microsites have an unaccounted role in soil carbon stabilization. Nature Communications 8, 1771.
Keller, J., Weisenhorn, P., Megonigal, P., 2009. Humic acids as electron acceptors in wetland decomposition. Soil Biology and Biochemistry 41, 1518–1522.
Klüpfel, L., Piepenbrock, A., Kappler, A., Sander, M., 2014. Humic substances as fully regenerable electron acceptors in recurrently anoxic environments. Nature Geoscience 7, 195.
Kramer, M.G., Sanderman, J., Chadwick, O.A., Chorover, J., Vitousek, P.M., 2012. Long-term carbon storage through retention of dissolved aromatic acids by reactive particles in soil. Global Change Biology 18, 2594–2605.
LaCroix, R.E., Tfaily, M.M., McCreight, M., Jones, M.E., Spokas, L., Keiluweit, M., 2019. Shifting mineral and redox controls on carbon cycling in seasonally flooded mineral soils. Biogeosciences 16, 2573–2589.
Li, S., Kappler, A., Zhu, Y., Haderlein, S.B., 2020. Mediated electrochemical analysis as emerging tool to unravel links between microbial redox cycling of natural organic matter and anoxic nitrogen cycling. Earth-Science Reviews 208, 103281.
Li, Y., Chen, Z., Chen, J., Castellano, M.J., Ye, C., Zhang, N., Miao, Y., Zheng, H., Li, J., Ding, W., 2022. Oxygen availability regulates the quality of soil dissolved organic matter by mediating microbial metabolism and iron oxidation. Global Change Biology 28, 7410–7427.
Lin, X., Zhang, Y., Sheng, Z., Huang, L., Gao, H., Wang, C., Wang, Y., 2022. A new strategy for preparation of high-performance onion-like anode material from coal tar pitch residue. Journal of Analytical and Applied Pyrolysis 166, 105591.
Liu, F., Zhu, K., Wang, Z., Liu, J., Ni, Z., Ding, Y., Zhang, C., Jia, H., 2023a. Production of reactive oxygen species and its role in mediating the abiotic transformation of organic carbon in sandy soil under vegetation restoration. Carbon Research 2, 35.
Liu, J., Hartmann, S.C., Keppler, F., Lai, D.Y.F., 2019. Simultaneous abiotic production of greenhouse gases (CO2, CH4, and N2O) in subtropical soils. Journal of Geophysical Research: Biogeosciences 124, 1977–1987.
Liu, J., Zhu, C., Liu, X., Wang, X., Zhou, D., 2023b. Nonmicrobial mechanisms dominate the release of CO2 and the decomposition of organic matter during the short-term redox process in paddy soil slurry. Eco-Environment & Health 2, 227–234.
Matus, F., Stock, S., Eschenbach, W., Dyckmans, J., Merino, C., Nájera, F., Köster, M., Kuzyakov, Y., Dippold, M.A., 2019. Ferrous wheel hypothesis: abiotic nitrate incorporation into dissolved organic matter. Geochimica et Cosmochimica Acta 245, 514–524.
Merino, C., Fontaine, S., Palma, G., Matus, F., 2017. Effect of aluminium on mineralization of water extractable organic matter and microbial respiration in southern temperate rainforest soils. European Journal of Soil Biology 82, 56–65.
Merino, C., Kuzyakov, Y., Godoy, K., Cornejo, P., Matus, F., 2020a. Synergy effect of peroxidase enzymes and Fenton reactions greatly increase the anaerobic oxidation of soil organic matter. Scientific Reports 10, 11289.
Merino, C., Kuzyakov, Y., Godoy, K., Jofré, I., Nájera, F., Matus, F., 2020b. Iron-reducing bacteria decompose lignin by electron transfer from soil organic matter. Science of The Total Environment, 143194.
Merino, C., Matus, F., Kuzyakov, Y., Dyckmans, J., Stock, S., Dippold, M.A., 2021. Contribution of the Fenton reaction and ligninolytic enzymes to soil organic matter mineralisation under anoxic conditions. Science of The Total Environment 760, 143397.
Mollhagen, A.C., Goodale, C.L., Martínez, C.E., 2021. Contrasting fates of nitrate between organic and iron oxide-rich horizons of an acidic forest soil under oxic and suboxic conditions. Soil Biology and Biochemistry 157, 108237.
Moursy, A., Ahmed, N., Sahoo, R., 2020. Determination of total content of some microelements in soil using two digestion methods. International journal of chemical studies 8, 2510–2514.
Murphy, K., Stedmon, C., Graeber, D., Bro, R., 2013. Fluorescence spectroscopy and multi-way techniques. PARAFAC. Analytical Methods 5.
Page, S.E., Kling, G.W., Sander, M., Harrold, K.H., Logan, J.R., McNeill, K., Cory, R.M., 2013a. Dark formation of hydroxyl radical in Arctic soil and surface waters. Environmental Science & Technology 47, 12860–12867.
Page, S.E., Kling, G.W., Sander, M., Harrold, K.H., Logan, J.R., McNeill, K., Cory, R.M., 2013b. Dark formation of hydroxyl radical in Arctic soil and surface waters. Environmental Science and Technology 47, 12860–12867.
Palma, G., Jorquera, M., Demanet, R., Elgueta, S., Briceño, G., de la Luz Mora, M., 2016. Urea fertilizer and pH influence on sorption process of Flumetsulam and MCPA acidic herbicides in a volcanic soil. Journal of Environmental Quality 45, 323–330.
Patzner, M.S., Mueller, C.W., Malusova, M., Baur, M., Nikeleit, V., Scholten, T., Hoeschen, C., Byrne, J.M., Borch, T., Kappler, A., Bryce, C., 2020. Iron mineral dissolution releases iron and associated organic carbon during permafrost thaw. Nature Communications 11, 6329.
Schlüter, S., Henjes, S., Zawallich, J., Bergaust, L., Horn, M., Ippisch, O., Vogel, H.-J., Dörsch, P., 2018. Denitrification in soil aggregate analogues-effect of aggregate size and oxygen diffusion. Frontiers in Environmental Science 6.
Seeberg-Elverfeldt, J., Schlüter, M., Feseker, T., Koelling, M., 2005. Rhizon sampling of pore waters near the sediment/water interface of aquatic systems. Limnology and Oceanography: Methods 3, 361–371.
Silver, W., Neff, J., McGroddy, M., Veldkamp, E., Keller, M., Oliveira Junior, R., 2000. Effects of soil texture on below ground carbon and nutrient storage in a lowland Amazon Forest ecosystem. Ecosystems 3, 193–209.
Slimani, I., Zhu-Barker, X., Lazicki, P., Horwath, W., 2023. Reviews and syntheses: iron – a driver of nitrogen bioavailability in soils? Biogeosciences 20, 3873–3894.
Stookey, L.L., 1970. Ferrozine—a new spectrophotometric reagent for iron. Analytical Chemistry 42, 779–781.
Totsche, K.U., Amelung, W., Gerzabek, M.H., Guggenberger, G., Klumpp, E., Knief, C., Lehndorff, E., Mikutta, R., Peth, S., Prechtel, A., Ray, N., Kögel-Knabner, I., 2018. Microaggregates in soils. Journal of Plant Nutrition and Soil Science 181, 104–136.
van Erk, M.R., Bourceau, O.M., Moncada, C., Basu, S., Hansel, C.M., de Beer, D., 2023. Reactive oxygen species affect the potential for mineralization processes in permeable intertidal flats. Nature Communications 14, 938.
Velikova, V., Yordanov, I., Edreva, A., 2000. Oxidative stress and some antioxidant systems in acid rain-treated bean plants: protective role of exogenous polyamines. Plant Science 151, 59–66.
Wang, C., Blagodatskaya, E., Dippold, M.A., Dorodnikov, M., 2022. Keep oxygen in check: contrasting effects of short-term aeration on hydrolytic versus oxidative enzymes in paddy soils. Soil Biology and Biochemistry 169, 108690.
Wang, S., Gao, W., Ma, Z., Zhu, Z., Luo, Y., Wei, L., Yuan, H., Chen, S., Ying, C., Mason-Jones, K., Kuzyakov, Y., Ge, T., 2024. Iron mineral type controls organic matter stability and priming in paddy soil under anaerobic conditions. Soil Biology and Biochemistry 197, 109518.
Wen, S., Lu, Y., Dai, J., Huang, X., An, S., Liu, J., Liu, Z., Du, Y., Zhang, Y., 2023. Stability of organic matter-iron-phosphate associations during abiotic reduction of iron. Journal of Hazardous Materials 449, 131016.
Werth, M., Kuzyakov, Y., 2010. 13C fractionation at the root–microorganisms–soil interface: a review and outlook for partitioning studies. Soil Biology and Biochemistry 42, 1372–1384.
Whalen, E.D., Grandy, A.S., Sokol, N.W., Keiluweit, M., Ernakovich, J., Smith, R.G., Frey, S.D., 2022. Clarifying the evidence for microbial- and plant-derived soil organic matter, and the path toward a more quantitative understanding. Global Change Biology 28, 7167–7185.
Wilhelm, R.C., Lynch, L., Webster, T.M., Schweizer, S., Inagaki, T.M., Tfaily, M.M., Kukkadapu, R., Hoeschen, C., Buckley, D.H., Lehmann, J., 2022. Susceptibility of new soil organic carbon to mineralization during dry-wet cycling in soils from contrasting ends of a precipitation gradient. Soil Biology and Biochemistry 169, 108681.
Wilmoth, J.L., 2021. Redox heterogeneity entangles soil and climate interactions. Sustainability 13, 10084.
Xiao, J., Guo, S., Wang, D., An, Q., 2024. Fenton-like reaction: recent advances and new trends. Chemistry - A European Journal 30, e202304337.
Xu, B., Lin, Z., Li, F., Tao, T., Zhang, G., Wang, Y., 2024. Local O_2 Concentrating Boosts the electro-Fenton Process for energy-efficient Water Remediation, vol.121. Proceedings of the National Academy of Sciences, e2317702121.
Yu, C., Xie, S., Song, Z., Xia, S., Åström, M.E., 2021. Biogeochemical cycling of iron (hydr-)oxides and its impact on organic carbon turnover in coastal wetlands: a global synthesis and perspective. Earth-Science Reviews 218, 103658.
Yu, G.-H., Kuzyakov, Y., 2021. Fenton chemistry and reactive oxygen species in soil: abiotic mechanisms of biotic processes, controls and consequences for carbon and nutrient cycling. Earth-Science Reviews 214, 103525.

Yudina, A.V., Klyueva, V.V., Romanenko, K.A., Fomin, D.S., 2022. Micro- within macro: how micro-aggregation shapes the soil pore space and water-stability. Geoderma 415, 115771.

Zhang, Y., Zhang, N., Qian, A., Yu, C., Zhang, P., Yuan, S., 2022. Effect of C/Fe molar ratio on H(2)O(2) and (•)OH production during oxygenation of Fe(II)-Humic acid coexisting systems. Environmental Science and Technology 56, 13408–13418.

Zhao, Y., Xiang, W., Huang, C., Liu, Y., Tan, Y., 2021. Production of hydroxyl radicals following water-level drawdown in peatlands: a new induction mechanism for enhancing laccase activity in carbon cycling. Soil Biology and Biochemistry 156, 108241.